Particle Accelerators, 1991, Vol. 35, pp. 15–42
Reprints available directly from the publisher
Photocopying permitted by license only

LONGITUDINAL BEAM COMPRESSION FOR HEAVY-ION INERTIAL FUSION

D. D.-M. HO, S. T. BRANDON

Lawrence Livermore National Laboratory, University of California, Livermore, California 94550, USA.

and

E. P. LEE

Lawrence Berkeley Laboratory, University of California, Berkeley, California 94720, USA.

(Received 16 October 1989; in final form 12 February 1990)

A scheme is described for compressing a heavy-ion beam longitudinally in such a way that the compressed pulse has uniform line-charge density and longitudinal momentum. Attaining these conditions will be important in the final focusing of a beam on a small fuel capsule in an inertial confinement fusion reactor. The longitudinal dynamics can be approximately described by a one-dimensional (1-D) fluid model for charged particles. Recognizing the similarity between the 1-D charged particle equations of motion and the 1-D equations for ideal-gas flow permits us to calculate the evolution of the line-charge density and velocity profile using self-similar solutions and the method of characteristics, developed for unsteady supersonic gas dynamics, for different regions along the beam. Simple physical arguments show that although the longitudinal and transverse temperatures vary along the beam following the adiabatic laws, no substantial longitudinal and transverse emittance growth is to be expected. Particle-in-cell simulations confirm all the physical arguments. The compressed beam has negligible longitudinal momentum spread and can therefore avoid chromatic aberrations in final focus.

1. INTRODUCTION

Heavy-ion induction linacs are receiving increased attention as drivers for commercial inertial confinement fusion (ICF)[1] because they can have high repetition rate ($\gg 1$ Hz),[2,3] high efficiency (up to 40%),[3] and good reliability over many pulses.

The achievable current in a linac is dependent on several factors, including number of beams, kinetic energy, and mass. However, it is not considered cost effective to accelerate the full current required for imploding high-gain ICF capsules. This is because it is easier to accelerate a long pulse, e.g., greater than 10 meters, than a short pulse, since an accelerating wave form has nonzero rise time. Moreover, the accelerator aperture radius should be kept reasonably small since transportable current is proportional to only the first power of the radius at a fixed pole-tip field.[4,5] Therefore, long pulses are employed. Consequently, in order to meet the final power requirement, e.g., 10^{15} W, for imploding high-gain capsules, the beam is compressed longitudinally by an order of magnitude or more before reaching the capsule.

Various authors have investigated the problem of longitudinal beam compression.

Haber[6] studied the compression of a pulse whose line-charge density is uniform in the middle of the pulse but falls off at the ends, and Hofmann and Bozsik[6] studied the compression of a pulse whose line-charge density is nearly uniform. Bisognano, Lee, and Mark[7] investigated the compression of a parabolic pulse. Mark *et al.*[8] carried out simulations of beam compression with pulse shaping. In all of these studies, the fully compressed beam did not have uniform particle longitudinal momentum and/or uniform line-charge density, both of which, and the former in particular, may be critical for final focusing. This is because the longitudinal momentum spread must be small (generally less than $\pm 1\%$) in order to focus a beam on a small (millimeter size) fuel capsule in a reactor without chromatic aberration. Further, in these studies, the emittance growth and the transverse beam dynamics during longitudinal compression were not investigated. An understanding of the emittance growth is important, since large growth makes it difficult to focus a beam on a small spot.

In this paper we give a detailed description of a method (briefly described in Refs. 9 and 10) for compressing a beam longitudinally in such a way that the bulk of the compressed beam has uniform longitudinal momentum and line-charge density. (Pulse-shaping can be obtained by delaying the arrival of some of the beams on the capsule or by upstream beam manipulations, which will be described in a forthcoming paper.) It is expected that both longitudinal and transverse emittances remain essentially constant during compression because both longitudinal and transverse temperatures vary along the beam during compression according to the adiabatic laws.[10] In the present work, particle simulations using CONDOR, a two-and-one-half dimensional (2-1/2-D) particle-in-cell (PIC) code, confirm these physical conjectures. The simulations also show that the 1-D fluid model of the beam longitudinal dynamics is a good approximation.

This paper is organized as follows. The compression scenario and the longitudinal beam dynamics are described in Section 2. In this section, we show that the beam motion can be described by fluid equations. The solutions to the fluid equations are self-similar in some regions of the beam, i.e., they do not depend upon the longitudinal spatial coordinate and time independently but are functions of the ratio of the two. In other region of the beam, the solutions are not self-similar, and there we employ the method of characteristics, developed for unsteady supersonic gas dynamics, to obtain the beam properties. In addition, an approximate solution is also obtained for this region. Section 3 discusses the transverse beam dynamics. Section 4 presents results from particle simulations, which confirm the discussions in the preceding sections. The results are summarized in Section 5. Appendix A outlines the theory underlying the method of characteristics and discusses the construction of the characteristics meshes for the 1-D "ion-fluid." Appendix B presents the scaling laws for beam transport, during longitudinal compression, in a focusing-defocusing (FODO) magnetic quadrupole transport channel. The implications of tune depression and an estimate of the total length of a typical beam compression section are given.

2. LONGITUDINAL DYNAMICS AND COMPRESSION SCENARIO

Compressing an ion beam longitudinally by an order of magnitude, such that the compressed configuration has uniform longitudinal momentum and line-charge

density profiles, requires specific upstream conditions on all the beam parameters. Section 2.1 discusses the method of obtaining those specific upstream conditions involving longitudinal beam parameters; fluid equations are used. To give an initially long and uniform beam such a profile, a number of beam-manipulation steps are needed. These steps—the "compression scenario" are described in Section 2.2.

2.1. Longitudinal Dynamics

To determine the upstream conditions for line-charge density λ, longitudinal velocity v_z, and longitudinal temperature T_z (see Fig. 1e), we investigate the equations for 1-D charged-particle motion in the beam-centered coordinates. The continuity equation is

$$\frac{\partial \lambda}{\partial t} + \frac{\partial \lambda v_z}{\partial z} = 0, \tag{1}$$

and the momentum equation is

$$\frac{\partial v_z}{\partial t} + v_z \frac{\partial v_z}{\partial z} = -\frac{Ze}{m} \frac{g}{4\pi\varepsilon_0} \frac{\partial \lambda}{\partial z}. \tag{2}$$

These equations assume non-relativistic dynamics, and quantities are defined in the beam reference frame. Here, e is the electronic unit of charge; ε_0 is the free-space permittivity; z is the longitudinal coordinate in the beam frame; m is the ion mass; Z is the ion charge state; $g = 2\ln(b/a)$ for a beam of radius a inside a perfectly conducting cylinder of radius b. Note that the expression for the space-charge force on the right-hand side of Eq. (2) is valid only if the scale length for variation in λ is larger than the beam radius.

The g factor is obtained by making three assumptions. (1) The beam charge density ρ is uniform and constant, i.e., the line charge density $\lambda = \pi a^2 \rho$ varies with z and t only through its dependence on $a(z, t)$. This corresponds to the limit of space-charge-dominated transport. (2) The beam radius is small compared with beam length. (3) The beam is contained by an azimuthally symmetric radial electric field $E(r) = E_0(r/a)$, where r is the radial coordinate. This unphysical field is a smooth limit approximation to the effect of a dense FODO system of magnetic quadrupoles. Note that $E(r)$ is assumed to be constant in time. The g factor is independent of r at any given time and hence so is the beam generated longitudinal electric field E_z inside radius a. But a, in general, varies along the beam and also changes with time. The fact that density is uniform and g is independent of r are the reasons that the 1-D Eqs. (1) and (2) can be used for the present problem. We find, however, that the value of g obtained from PIC simulations (see Section 4) differs considerably from that obtained from the simple formula given above.

Note that in Eq. (2), the gradient of thermal pressure is not included since it is small compared with the electrostatic force for the cases under consideration. The ratio of these two forces is

$$\frac{(1/\rho)(\partial P/\partial z)}{(Ze/m)(g/4\pi\varepsilon_0)(\partial\lambda/\partial z)} \simeq 0\left(\frac{4\pi\varepsilon_0 T_z}{Ze\lambda g}\right), \tag{3}$$

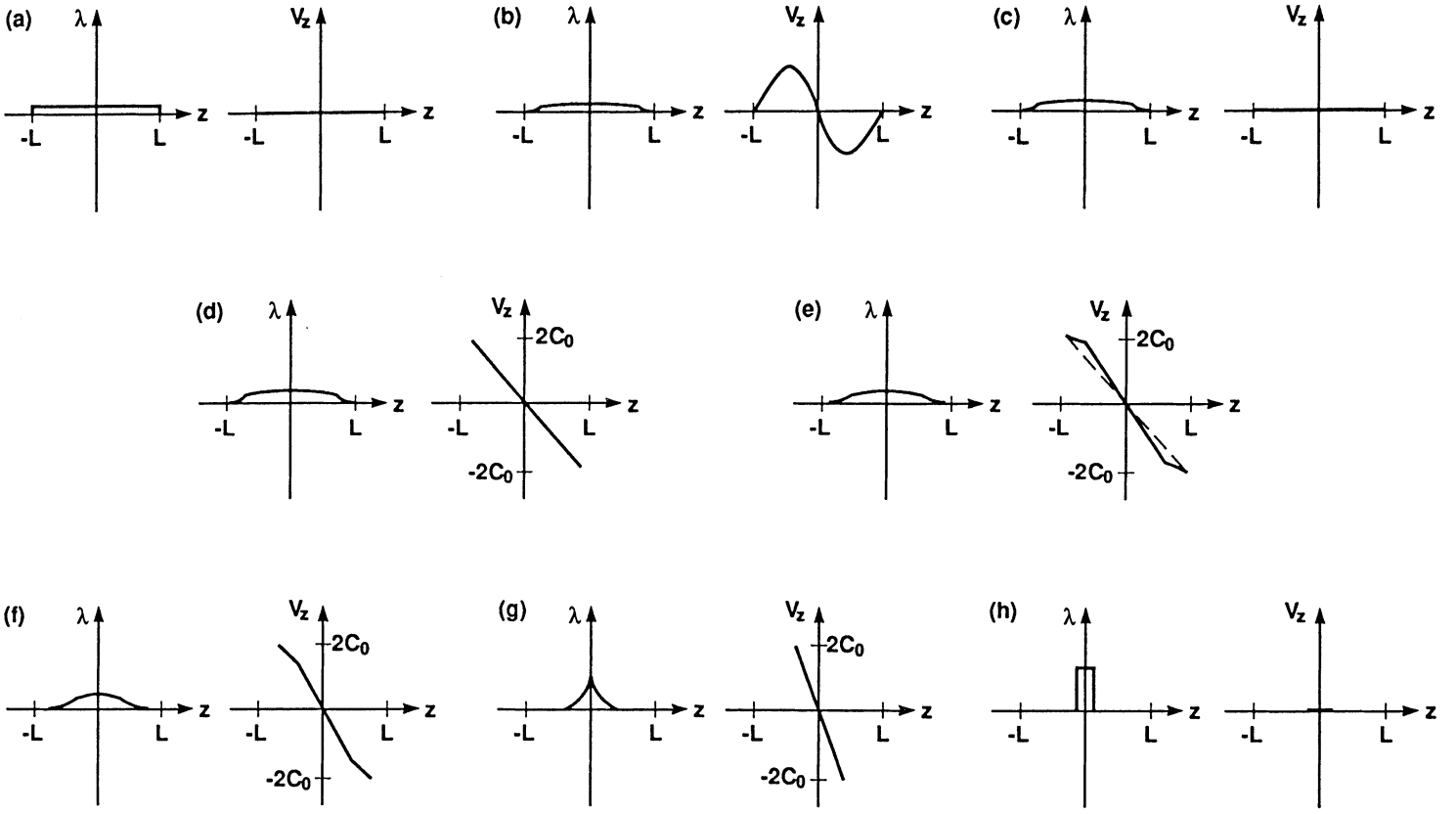

FIGURE 1 Compression scenario. (a) Initial uniform line-charge density λ and longitudinal velocity v_z (in beam-centered coordinates). (b) Imposing a proper velocity tilt to shape the line-charge density profile. (c) The desired line-charge density profile is achieved and the velocity tilt is removed. (d) A linear velocity tilt is imposed. (e) "Mid-course" correction of the velocity tilt. (f) Beam undergoes self-compression. (g) At an intermediate time during self-compression, the simple-wave region extends the entire length of the beam and the velocity tilt becomes linear. (h) The self-compression is complete and the beam has uniform line-charge density and longitudinal velocity.

TABLE I

Typical Heavy-Ion Beam Parameters for an Inertial Fusion Driver.

Ion mass	210 amu
Ion charge state	+3
Ion kinetic energy	11.5 GeV
Before compression	
Beam length	15 m
Line charge density, λ	4.59×10^{-6} C/m
Longitudinal temperature, T_z	0.044 keV
Normalized rms transverse emittance $\bar{\varepsilon}_n$	3.8 μm·rad
After compression (ideal values)	
Beam length	1 m
Line charge density, λ	6.88×10^{-5} C/m
Longitudinal temperature, T_z	10 keV
Normalized rms transverse emittance $\bar{\varepsilon}_n$	3.8 μm·rad

where P is the thermal pressure. Using the final beam parameters given in Table 1, the above expression shows that the ratio of the forces is in the range between $0(10^{-3})$ and $0(10^{-4})$. If the beam charge state changes from +3 to +1, the ratio of the two forces increases by an order of magnitude, yet it is still small, i.e., $0(10^{-2})$. Note that in the table, the initial longitudinal temperature T_z of the beam is set by its value in the final, compressed configuration. This "compressed" T_z is limited by the maximum value that can satisfy the constraint, imposed by chromatic aberration, for final focusing. For example, to focus kiloampere beams onto a millimeter-size spot, the longitudinal momentum spread should be no more than $\pm 10^{-3}$.[3] This spread corresponds to a compressed temperature of about 10 keV for a 10-GeV beam.

Equations (1) and (2) are identical to the equations for 1-D ideal fluid motion, except that the pressure force in the fluid equation is replaced by the electrostatic force in Eq. (2). Note that Eqs. (1) and (2) are invariant under the simultaneous reversal of signs of t and v_z. Thus, the longitudinal beam compression (between Figs. 1e and 1h) can be treated by analogy with the time-reversible process for the free expansion of a slab of gas having a ratio of specific heat $\gamma = 2$ and with initially uniform density and pressure profiles.

When a uniform beam starts to expand longitudinally (Fig. 1h), the leading edges of the rarefaction waves, where $v_z = 0$, start at the two ends of the beam and propagate along the trajectories $z = \pm L \mp c_0 t$ toward the beam center; the trailing edges of the waves move away from the beam at the escape speed with magnitude $2c_0$. Here L is half of the initial total length of the beam, which is centered at $z = 0$. The wave speed c is given by

$$c = \sqrt{\frac{Ze}{4\pi\varepsilon_0}\frac{g\lambda}{m}}, \tag{4}$$

and c_0 is the wave speed when λ is at its maximum value λ_0.

After the leading edges meet at the beam center at time $t_0 = L/c_0$ (Fig. 1g), the boundary that separates the central wave overlapping region from the region without

overlapping, for the left-half of the beam, propagates away from the beam center following the trajectory[11]

$$z_b = -2c_0 t + 3L\left(\frac{t}{t_0}\right)^{1/3} - L, \quad t \geq t_0. \tag{5}$$

Note that as $t \gg t_0$, $\partial z_b/\partial t$ approaches the escape speed.

In the regions where the rarefaction waves do not overlap, the waves are simple waves[11,12] since the characteristics launched by the disturbance at $z = \pm L$ do not cross each other (see discussion in Appendix A). In the region where overlap occurs, the rarefaction waves are nonsimple, since characteristics cross. For an initially uniform beam, Eqs. (1) and (2) in the simple wave regions have an analytical solution if the g factor is treated as a constant independent of z. The justification for treating the g factor as a constant is given in Appendix A. The time evolution of λ and v_z (for the left-half of the beam) can then be expressed as:

$$\frac{\lambda}{\lambda_0} = \begin{cases} 1, & z > c_0 t - L, \quad 0 < t < t_0, \\ \left(\frac{2}{3} + \frac{z+L}{3c_0 t}\right)^2, & \begin{cases} -2c_0 t - L < z < c_0 t - L, & 0 < t \leq t_0, \\ -2c_0 t - L < z < z_b, & t > t_0, \end{cases} \\ 0, & z < -2c_0 t - L, \quad t > 0, \end{cases} \tag{6}$$

$$\frac{v_z}{c_0} = \begin{cases} 0, & z > c_0 t - L, \quad 0 < t \leq t_0, \\ -\frac{2}{3}\left(1 - \frac{z+L}{c_0 t}\right), & \begin{cases} -2c_0 t - L < z < c_0 t - L, & 0 < t < t_0, \\ -2c_0 t - L < z < z_b, & t > t_0. \end{cases} \end{cases} \tag{7}$$

These equations are obtained by shifting the spatial coordinate and the time origin of the self-similar simple wave solutions given in Refs. 11–13. We note from Eq. (6) that the amount of charge in the simple-wave region is decreasing with time for $t > t_0$.

After the rarefaction waves meet at the beam center, the λ and v_z profiles in the nonsimple-wave region can be obtained graphically using the method of characteristics (described in Appendix A); there is no analytical solution for a gas with $\gamma = 2$. However, the characteristics mesh depicted in Fig. 6a (Appendix A) shows that the characteristics in the nonsimple-wave region are very close to straight lines as long as the time is not very much greater than t_0. This suggests that v_z should be very close to a linear function in z (see Appendix A for an explanation), which is indeed confirmed by simulations discussed in Section 4. Linearity of v_z in z allows us to construct an approximate solution for λ in the nonsimple-wave region.

Assume v_z varies as $F(t)z$. Then, matching this function to the velocity in the simple-wave region at z_b gives

$$v_z(z, t) = -2\left[1 - \left(\frac{t}{t_0}\right)^{-2/3}\right] c_0\left(\frac{z}{z_b}\right), \quad z \geq z_b, \; t \geq t_0. \tag{8}$$

Comparing this result to the v_z obtained from the method of characteristics using Figs. 6a and 6b shows that at $t = 2t_0$ the agreement is within 3% at a position $z = -0.6L$. Note that the value of $\partial v_z/\partial z$ obtained from this equation and the value

of $\partial v_z/\partial z$ in the simple-wave region at $z = 0$ as t/t_0 approaches unity are $(4/3)(c_0/L)$ and $(2/3)(c_0/L)$, respectively. These value are not the same because the fluid motion in the simple-wave and in the nonsimple-wave regions behaves differently.

Using Eq. (8) and the momentum equation, we can now obtain λ and then match its value to the value of λ in the simple-wave region at z_b. The result is

$$\lambda(z,t) = \lambda_0\left(\frac{t}{t_0}\right)^{-4/3} + \lambda_0\left[\frac{2}{3}\left(\frac{t}{t_0}\right)^{-5/3} - \left(\frac{t}{t_0}\right)^{-4/3} + \frac{1}{3}\left(\frac{t}{t_0}\right)^{-2/3}\right] \times\left[1 - \left(\frac{z}{z_b}\right)^2\right], \qquad z \geq z_b,\ t \geq t_0. \tag{9}$$

Comparing the values of λ obtained from this equation to those obtained from Fig. 6(a) shows that at $t = 2t_0$, the difference in λ obtained from the two methods agrees within 1% at $z = 0$.

Another way to check the accuracy of Eq. (9) is to compare the total charge inside the nonsimple-wave region calculated by Eq. (9) to the result obtained by subtracting the charge in the simple-wave region obtained from Eq. (6) from the total charge. This again shows excellent agreement; e.g., at $t = 2t_0$, the agreement is within 0.5%.

Since λ and v_z given by Eqs. (8) and (9) are approximate solutions, they do not satisfy the continuity equation. However, if we use the approximate values of λ and v_z in the continuity equation, we find that the cancellation between the $\partial\lambda/\partial t$ and the $(\partial/\partial z)(v_z\lambda)$ terms is within 4% of $\partial\lambda/\partial t$ at $z = 0$ at $t = 2t_0$. From this, we conclude that Eqs. (8) and (9) are good approximations of λ and v_z in the nonsimple-wave region at $t = 2t_0$. However, the errors resulting from the approximate solutions increase with time. For example, at $t = 3t_0$, the value of the charge inside the nonsimple-wave region obtained from the approximate formula differs from the actual value by about 2%. This suggests that Eqs. (8) and (9) should be able to approximate the beam properties with reasonable accuracy for $t \leq 3t_0$.

Using Eqs. (6) and (7) together with either Eqs. (8) and (9) or the characteristics meshes (Figs. 6a and 6b), we obtain the λ and v profiles of a beam of length 10L resulting from the longitudinal expansion of a uniform beam of length 2L; these profiles are plotted versus z in Fig. 2.

Another method to obtain λ in the nonsimple-wave region, employed by D. L. Judd,[14] is again to assume that v_z varies as $F(t)z$ and then solve the coupled Eqs. (1) and (2) for $F(t)$ and λ. Judd found that the solutions obtained by this method agree closely with the approximate solutions described above.

The behavior of the longitudinal emittance ε_z (microscopic phase area) and longitudinal temperature T_z are readily determined from the model features. Also, as mentioned earlier, E_z is independent of radius at any given z. Consequently, ε_z is essentially constant in time. This implies that the longitudinal temperature follows the 1-D adiabatic compression law, i.e.,

$$T_z = T_z^0\left(\frac{\lambda}{\lambda_0}\right)^2, \tag{10}$$

with initial longitudinal temperature T_z^0 and initial line-charge density λ_0.

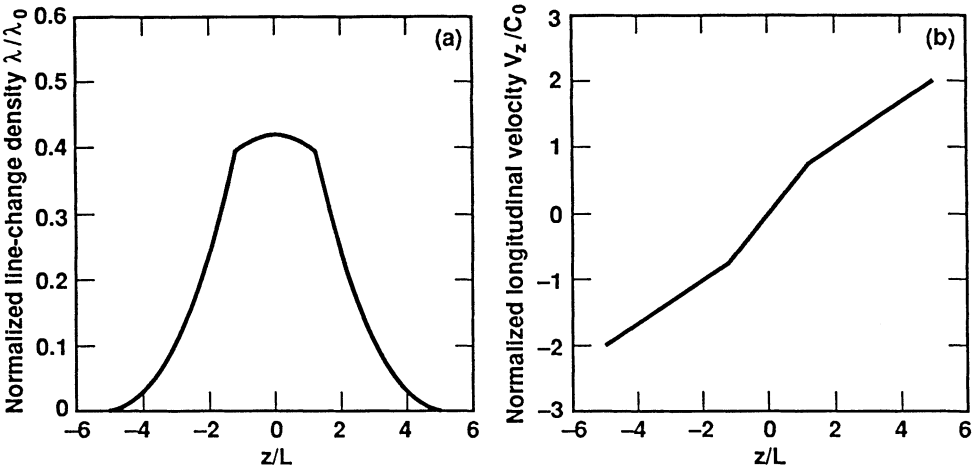

FIGURE 2 Line-charge density and velocity-tilt profiles of a beam with length $10L$ resulted from the expansion of a uniform beam with initial length $2L$. (a) Line-charge density vs. z. (b) longitudinal velocity vs. z.

2.2 Compression Scenario

To change a long, uniform beam (Fig. 1a) into the configuration specified by Fig. 1e, the beam-manipulation procedure consists of the following three steps: (1) establish the appropriate λ profile from an initially uniform beam, (2) impose a linear velocity tilt, and (3) establish the desired velocity profile. We now discuss each of these steps in turn.

(1) Establish the appropriate λ profile from an initially uniform beam. During acceleration, λ can be assumed to be constant except for the short rise and fall at the ends. The space-charge effect (i.e., the longitudinal electrostatic force that results from the gradient of λ) is relatively weak, because the beam pulse is still long (greater than 10 m). Under these circumstances, the constant-λ profile can be changed to any other reasonable shape by giving the beam a suitable velocity tilt. This can be understood by first writing the continuity equation in the Lagrangian coordinate, i.e.,

$$\frac{\partial \Gamma}{\partial t} = \frac{\partial v_z}{\partial m}, \tag{11}$$

where $\Gamma = 1/\lambda$, $dm = \lambda dz$, and $\partial/\partial t$ means $\partial/\partial t + v_z \partial/\partial z$ here.

If space charge is not important, then v_z is almost constant in time for each particle after the required velocity tilt is imposed. If the desired pulse shape is achieved in time τ, then after integrating Eq. (11) in time and converting to the Eulerian coordinate we have

$$\left.\frac{\partial v_z(z)}{\partial z}\right|_\tau = \left[1 - \frac{\lambda(z,\tau)}{\lambda(z,0)}\right]\frac{1}{\tau}. \tag{12}$$

Since the initial line-charge density profile $\lambda(z, 0)$ is constant along z and $\lambda(z, \tau)$ is given, the required velocity-tilt profile $v_z(z, \tau)$ to achieve $\lambda(z, \tau)$ can be obtained from

Eq. (12). Once $v_z(z, \tau)$ is known, $v_z(z, 0)$ can be obtained by linear transformation of $v_z(z, \tau)$ back to $\tau = 0$ since v_z at each slice along z is nearly constant.

In Fig. 1a, the uniform beam is assumed to have no velocity tilt in the accelerator. A tilt is gradually imposed on the beam through appropriate wave forms on the accelerating gaps. This tilt reaches a maximum in Fig. 1b and is removed gradually afterwards, again by means of appropriate wave forms on the accelerating gaps. Tilt removal is complete when the desired λ profile is achieved in Fig. 1c.

Note that this scheme is feasible only if the upper limit on the time τ, which is set by the time when the space-charge effect becomes important, is greater than the lower limit on τ, which is set by engineering limits, i.e., the shortest time in which the required longitudinal momentum variation can be induced by the induction cores. This turns out, indeed, to be the case, as we now show.

The expression for the maximum velocity $v_{z\max}$ of the velocity profile required to set up the specified λ profile can be obtained in the following way. First we obtain the location of $v_{z\max}$ by setting $\partial v_z/\partial z = 0$ in Eq. (12) and using Eq. (6) for the expression for $\lambda(\tau, z)$. If the initial beam length is fifteen times the compressed beam length, then the locations of $\pm v_{z\max}$ are inside the simple-wave regions. Thus, $v_{z\max}$ can be obtained by inserting Eq. (6) into Eq. (12) and then integrating Eq. (12) from the beam end to the location of $v_{\max}$. We find

$$v_{z\max} = -\frac{3.71L}{\tau}. \tag{13}$$

The constraint for time τ is that during this time, the space-charge effect should not greatly degrade the desired pulse shape. We assume that this condition is satisfied if the distance s of any particle moved by the electrostatic force along the beam is less than half of a percent of the total beam length during τ. In estimating τ, we assume the average electrostatic acceleration $\bar{a}$ to be half of the acceleration due to the maximum line-charge density gradient $\partial\lambda/\partial z|_{\max}$ at time τ. The location of $\partial\lambda/\partial z|_{\max}$ is at the boundary between the simple- and nonsimple-wave regions. Using the parameters given in Table 1 for a 15-m-long beam and the expression $S = (1/2)\bar{a}\tau^2$ for the distance travelled under constant acceleration $\bar{a}$, the time for a particle to move a distance S is found to be approximately 2.0 μs. Taking into account the time required to set up and then remove the velocity tilt, we let the value of τ used in Eq. (13) be half of the τ value just calculated. Thus, $L = 0.5$ m gives $v_{z\max} \simeq 2 \times 10^6$ m/s. Near the end of the accelerator, the maximum possible beam energy increment is about one MeV/m times the ion charge state.[15] Hence, the time required to set up a velocity tilt with $v_{z\max} \simeq 2 \times 10^6$ m/s is about 10^{-6} s. This simple analysis shows that it is possible to set up the required velocity tilt well before the pulse shape is degraded by the space-charge effect.

Thus far, we have obtained the velocity-tilt profile from Eq. (12) by assuming that $v_z(z, 0)$ can be imposed instantaneously. The detailed procedure for creating the desired line-charge density profile, with the consideration that it requires nonzero time to establish the desired velocity-tilt profile, needs further study.

(2) Impose a linear velocity tilt. A linear velocity tilt is now gradually given to the beam until the peaks of the tilt reach $\pm 2c_0$. The beam, as shown in Fig. 1d, is now

shorter than it was in Fig. 1c, because of the compression resulting from the linear velocity tilt. However, compressing the beam by a linear velocity tilt does not alter the functional form of λ.

(3) Establish the desired velocity profile. At this point, a "mid-course correction" is given to the beam to change the linear velocity profile to that specified in Fig. 1e. The shape of the λ and v_z profiles shown in Fig. 1e are obtained from the method described in Section 2.1 (except that the slope of the velocity-tilt is opposite) by using the time-reversal of the expansion process between Figs. 1e and 1h. Since the velocity difference between desired velocity profile and the linear profile (i.e., the difference between the dotted and solid lines in Fig. 1e) is small, the mid-course correction can be carried out so rapidly that the functional form of λ in Fig. 1e remains essentially the same after the change.

No more external manipulation of the beam is required beyond Fig. 1e. Figure 1f shows the λ and v_z profiles of the beam as the beam leaves the accelerator and enters the drift-compression section. The beam having these profiles compresses itself in such a way that the electrostatic force generated by the gradient of λ removes all the velocity tilt at the end of the compression, as shown in Fig. 1h. (Note that Fig. 1g shows the instant when the nonsimple-wave region disappears, i.e., the time when the leading edges of the simple waves meet at the beam center.)

All the discussions and physical arguments described in this section are confirmed by particle simulations presented in Section 4.

3. TRANSVERSE DYNAMICS

In this section we discuss the beam transverse density profile, the radial motion of the beam envelope, the variation of transverse temperature along the beam, and the transverse emittance. It is necessary to understand these functions in order to set up the beam initial conditions for particle simulation.

We first show that in an applied linear focusing-force field, e.g., a FODO field, the transverse beam density profile remains uniform, with or without simultaneous longitudinal compression, if the initial profile is uniform. We start with the continuity and transverse momentum equations with applied linear magnetic focusing forces for a cold beam, i.e.,

$$\dot{n} + \nabla \cdot n\bar{v} = 0, \tag{14a}$$

$$\dot{\bar{v}} + \bar{v} \cdot \nabla \bar{v} = \begin{cases} -k_x x + \dfrac{Ze\lambda}{\pi\varepsilon_0 \gamma^3 m a_x (a_x + a_y)} x, & \text{in the } x \text{ direction} \\ -k_y y + \dfrac{Ze\lambda}{\pi\varepsilon_0 \gamma^3 m a_y (a_x + a_y)} y, & \text{in the } y \text{ direction.} \end{cases} \tag{14b}$$

Here, n is the number density, a_x and a_y are the semiaxes of a beam with elliptical cross section, and $k_x x$ and $k_y y$ are the applied forces and are generally functions of z.

Now assume that the velocities in the x, y, and z directions have the forms

$$v_x = \frac{\dot{a}_x}{a_x} x, \tag{15a}$$

$$v_y = \frac{\dot{a}_y}{a_y} y, \tag{15b}$$

$$v_z = -v_{z0} z. \tag{15c}$$

Here v_{z0} is a constant and the dot represents a time derivative of the quantity. Substituting these expressions into Eqs. (14a) and (14b) and assuming n is a function of time only, we obtain

$$\dot{n} + n\left(\frac{\dot{a}_x}{a_x} + \frac{\dot{a}_y}{a_y} - v_{z0}\right) = 0, \tag{16a}$$

$$\ddot{a}_x = -k_x a_x + \frac{Ze\lambda}{\pi\varepsilon_0 \gamma^3 m(a_x + a_y)}, \tag{16b}$$

$$\ddot{a}_y = -k_y a_y + \frac{Ze\lambda}{\pi\varepsilon_0 \gamma^3 m(a_x + a_y)}. \tag{16c}$$

Thus, if the initial density profile is uniform, then it is uniform for all time since Eq. (16a) is independent of transverse coordinates while Eqs. (16b) and (16c) are just the envelope equations for a cold beam with elliptical cross section and uniform density.

We now show that the beam envelope does not have mismatch oscillations during longitudinal compression. This can be shown by using the envelope equation for a beam having circular cross section with radius a in a uniform linear external field, i.e.,

$$\frac{\partial^2 a}{\partial z^2} = -\bar{k}_0 a + \frac{Q}{a}. \tag{17}$$

Here the average applied force per unit mass from the FODO structure is given by $-\bar{k}_0 a$, with[16,17]

$$\bar{k}_0 \simeq \frac{3 - 2n}{6} \eta^2 k_0^2 l^4, \tag{18}$$

where η is the fractional occupancy of quadrupoles, l is the half period length of a FODO structure, and $k_0 \equiv B'/[B\rho]$ is the usual quadrupole strength for particles with magnetic gradient B' and magnetic rigidity $[B\rho]$. The generalized perveance Q is given by

$$Q = \frac{Ze\lambda}{2\pi\varepsilon_0 \beta^2 \gamma^3 mc^2}. \tag{19}$$

Note that B', η, and L can in general be functions of s (the laboratory coordinate in the the direction of beam propagation), while $[B\rho]$, λ, and β can be function of z and t.

The increase in line charge density due to longitudinal compression, after the beam travels through a typical FODO structure with a length of a few meters, is small,

e.g., a few percent. Therefore, if the beam is initially in radial force equilibrium, the acceleration term $\partial^2 a/\partial z^2$ in the beam frame is small compared with force terms on the right-hand side of Eq. (17). Thus, the beam is in approximate transverse force equilibrium, i.e.,

$$a \simeq \sqrt{\frac{Q}{k_0}}. \tag{20}$$

The radial motion is adiabatic and consequently there are no envelope mismatch oscillations during longitudinal compression. Note that although the longitudinal compression rate is different along different parts of the beam (because the velocity tilt along the beam is different, as shown in Fig. 1e) and hence different slices tend to expand at different rates, the influence of the external field tends to keep the envelope along different parts of the beam evolving according to Eq. (20).

Equation (20) implies that in a channel with a uniform and time-independent applied linear focusing field, the beam density is essentially the same everywhere inside the beam except near the ends and is incompressible during longitudinal compression. In a FODO system, however, the density along the beam is not the same at any given time. But for an observer seeing the beam passing a fixed location in the laboratory frame, the beam appears to have essentially constant density.

Our discussions, so far, have been limited to cold beams. This is a good approximation for the beam under consideration here since the beam in the transport channel is space-charge dominated, i.e., the space-charge force is much greater than the thermal pressure. Thus, the beam density profile is uniform up to a thin region—the Debye sheath, of thickness λ_D—at the beam edge.

The Debye thickness λ_D is given approximately by $(1/8)(\sigma/\sigma_0)a$ (Ref. 18) for beams in a linear external field. Here $\sigma(\sigma_0)$ is the single-particle phase advance (degrees per focusing period) with (without) space charge. For the space-charge-dominated beams under consideration here, $\sigma/\sigma_0 < 0.1$ and $\lambda_D/a < 0(10^{-2})$. Thus, beam density is uniform for most of the beam. Note that although the ratio λ_D/a can approach unity near the beam ends, where σ/σ_0 is not small, the volume of these regions is small and hence these regions are not important. Therefore, we use Eq. (20) to calculate the beam envelope in setting up the initial conditions for the particle simulation in Section 4, except near the beam ends. In estimating the envelope size near the beam ends, we use the envelope equation including the emittance term.

The fact that the beam profile remains essentially uniform suggests that the effective normalized emittance $\varepsilon_n = \beta\gamma\varepsilon$ is an invariant. This feature is predicted by Wangler's equation for emittance growth,[19]

$$\frac{d\varepsilon^2}{dt} = -\frac{a^2 Q}{2u_0}\frac{dE}{dt}. \tag{21}$$

where $u_0 \equiv (\lambda/Z)^2/4\pi\varepsilon_0$ and E is the difference in space-charge field energy of a beam with and without uniform profile. For the present case, dE/dt always equals zero.

However, as shown in Section 4, the emittance does grow at the beam ends during compression. One may be tempted to think that this may be due to the fact that λ

is small near the beam ends; hence the thermal force dominates rather than the space-charge force. If the thermal force dominates, the density profile is nonuniform and emittance grows according to Eq. (21). However, $d\varepsilon^2/dt$ is proportional to λ which is small at beam ends. Hence the amount of emittance growth according to Eq. (21) is insufficient to account for that observed in Section 4. Therefore, the observed emittance growth at the ends is probably caused by other effects.

The mean square emittance can be expressed as[20]

$$\varepsilon_x^2 = \langle x^2 \rangle \langle T_\perp \rangle + [\langle x^2 \rangle \langle U^2 \rangle - \langle xU \rangle^2], \tag{22}$$

where $T_\perp$ is the dimensionless beam transverse temperature and U is the dimensionless radial fluid velocity. For the typical heavy-ion beams considered here, $\langle U^2 \rangle / \langle T_\perp \rangle \sim 0(10^{-1})$. Thus, $\varepsilon_x^2 \sim \langle x^2 \rangle \langle T_\perp \rangle$ and consequently, constancy of ε_n gives the variation of transverse temperature $T_\perp$ with radius, i.e.

$$T_\perp = T_\perp^0 \left(\frac{a_0}{a(z)} \right)^2, \tag{23}$$

where $T_\perp^0$ is the initial transverse temperature and a_0 is the initial radius. Equation (23) is the 2-D adiabatic compression law with $\gamma = 2$. Note that $a(z)$ can be calculated from Eq. (20) if λ, which is determined from longitudinal dynamics, is known.

All the discussions and physical arguments presented in this section are confirmed by the particle simulations described in the following section.

4. PARTICLE SIMULATION

Particle-in-cell simulation has been used to check the simple fluid model described above. A beam with the parameters listed in Table I was used in the simulations. The feasibility of pulse shaping discussed in Section 2 is demonstrated in Section 4.1. In Section 4.2 we show that given the proper initial profiles of line-charge density and velocity tilt, a beam can be compressed by an order of magnitude, with the compressed configuration having essentially constant line-charge density and a vanishing velocity tilt.

4.1. Simulation of Pulse-Shaping

To demonstrate the feasibility of pulse shaping from an initially rectangular pulse, we choose the final pulse shape to be parabolic so that Eq. (12) can be analytically integrated for $v_z(z)$. If the beam is initially 15 m long, then the maximum allowable time τ, which is set by the criterion that during this time, the space-charge effect should not greatly degrade the desired pulse shape, is found to be about 10^{-6} s for changing the pulse to a pulse with the same length but with parabolic λ profile. Knowing τ and using Eq. (12), $v_z(z, \tau)$ can be calculated and $v_z(z, 0)$ can be obtained by projecting $v_z(z, \tau)$ back to $t = 0$. Figure 3a shows the initial uniform λ profile along the beam and Fig. 3b shows $v_z(z, 0)$ versus z. The fluctuations in Fig. 3a are caused by the finite number of particles in each simulation cell.

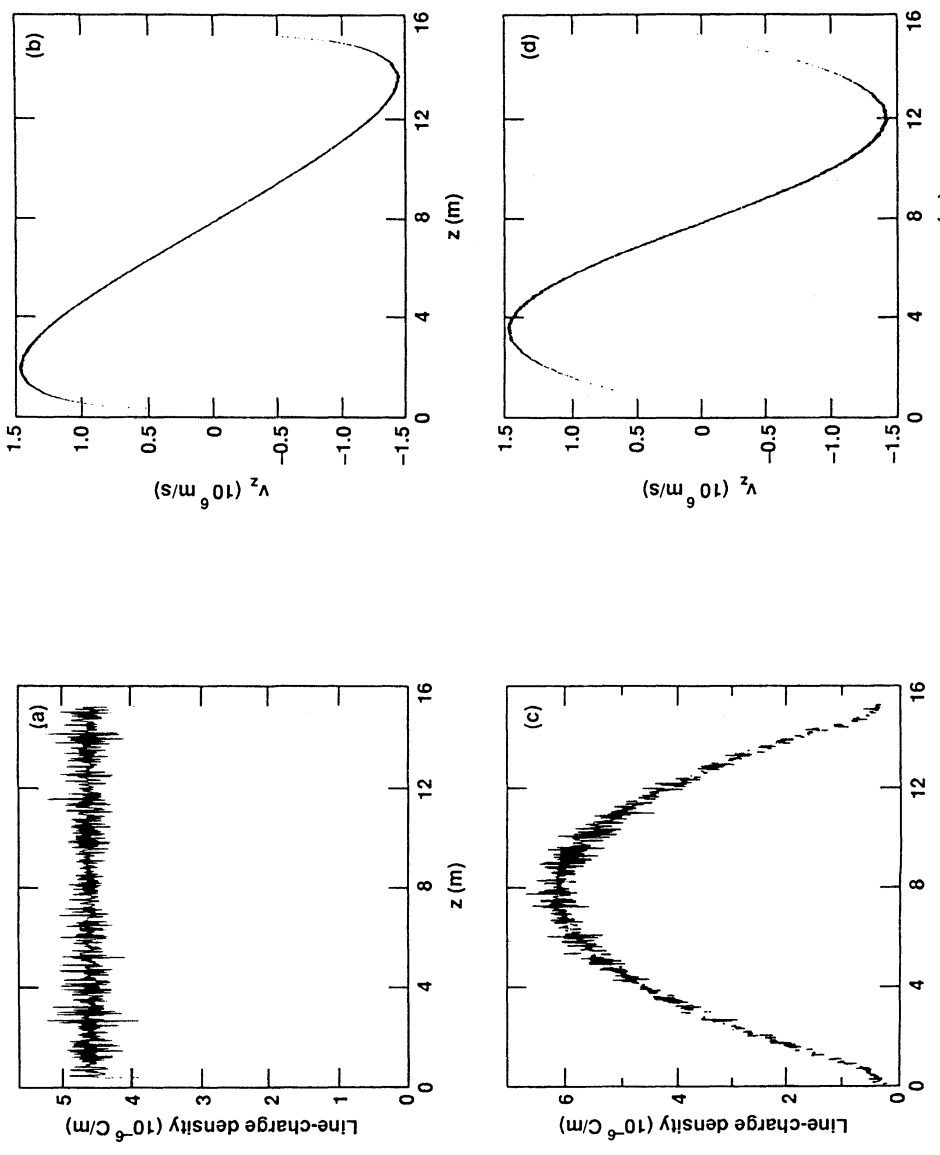

FIGURE 3 Particle simulation of pulse shaping. (a) Initial line-charge density. (b) Initial velocity tilt. (c) Final line-charge density (parabolic line-charge density profile has been achieved). (d) Final velocity tilt.

In the CONDOR PIC simulation, the beam is represented by 4×10^4 test particles. The beam has an initial radius $a = 3$ cm and the longitudinal and transverse temperatures (Gaussian particle distribution in velocity space) are 44.44 and 6200 eV, respectively. The radial boundary condition is that of a cylindrical perfect conductor at a radius $b = 6$ cm. The quadrupole magnetic field is represented by an azimuthally symmetric radial electric field $E(r) = E_0(r/a)$ that is independent of z and t.

After 10^{-6} s, the pulse does change from the initial uniform λ profile into the desired parabolic profile shown in Fig. 3c. Within the accuracy of this particle simulation, the shape of the parabolic profile is exactly the same as the calculated profile, except very near the ends of the beam. The shape of the velocity profile at the corresponding time is shown in Fig. 3d.

4.2 Simulation of Self-Compression

We now show the feasibility of compressing a beam such that the final configuration has uniform v_z and λ and a length of 1 m. We start the simulation when the beam is 5 m long. (The compression from 15 m to 5 m was not simulated because the physics is the same for compression from 5 m to 1 m. In addition, the available amount of computer time was limited.) The λ profile for the 5-m-long beam is shown in Fig. 2a, while the velocity profile required to compress the beam is the same as that given in Fig. 2b but with opposite slope. We then use these profiles as the initial conditions for PIC simulations (Fig. 4a and 4c).

Note that the actual peak-to-peak values of the velocity tilt used in the input of simulation are about 50% greater than that obtained from Eq. (7). This discrepancy is probably due to the fact that the simple expression for the g factor given in Section 2.1 cannot model the multi-dimensional effects near the beam ends accurately and the fact that $\partial\lambda/\partial z$ varies rapidly near the ends.

Knowing the λ profile and using the equilibrium envelope equation (setting $\partial^2 a/\partial^2 z = 0$), the beam radius can be obtained. The calculated particle distribution within the beam envelope (particle density is constant inside the beam except near ends) is shown in Fig. 4b. Near the ends of the beam, the radius expands to about twice the calculated value (with constant density profile) after approximately 10^{-8} s. This is due to the fact that the density profile becomes nonuniform near the ends because at these locations, the beam is no longer space-charge-dominated. The longitudinal and transverse temperatures can be obtained using Eqs. (10) and (23); $T_\perp$ and T_z versus z are plotted in Figs. 4d and 4e, respectively. Note that the existence of T_z is also evident on the v_z versus z plot as shown in Fig. 4c. In the absence of T_z, v_z versus z would be just a zero-width line.

The initial beam parameters specified above provide the initial conditions for CONDOR PIC code. About 4×10^4 particles are used to simulate the self-compression. About 500 grid cells are used in the longitudinal direction, and the radial direction is divided into about 300 zones. The initial spread of the transverse velocity v_x is plotted versus x in Fig. 4f; this plot is nearly identical to the plot for v_y versus y, because of axial symmetry. Note that on this plot, there are particles with relatively high v_x around $x = 0$. This is because particles at the ends have higher transverse temperature and are contained in areas with small radius. However, the

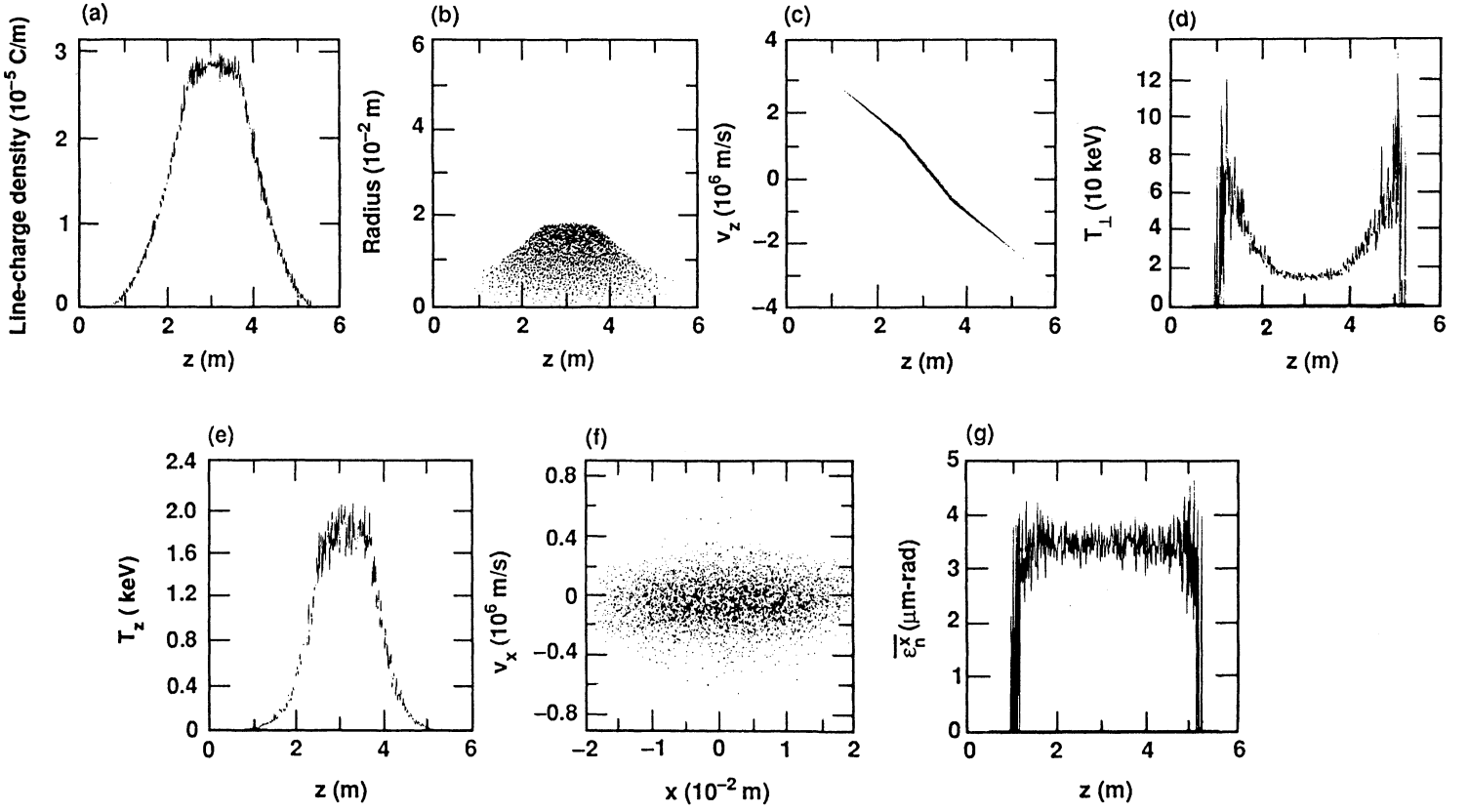
(a)
Line-charge density (10^{-5} C/m)
z (m)
(b)
Radius (10^{-2} m)
z (m)
(c)
v_z (10^6 m/s)
z (m)
(d)
$T_\perp$ (10 keV)
z (m)
(e)
T_z (keV)
z (m)
(f)
v_x (10^6 m/s)
x (10^{-2} m)
(g)
$\overline{\varepsilon_n^x}$ (μm-rad)
z (m)

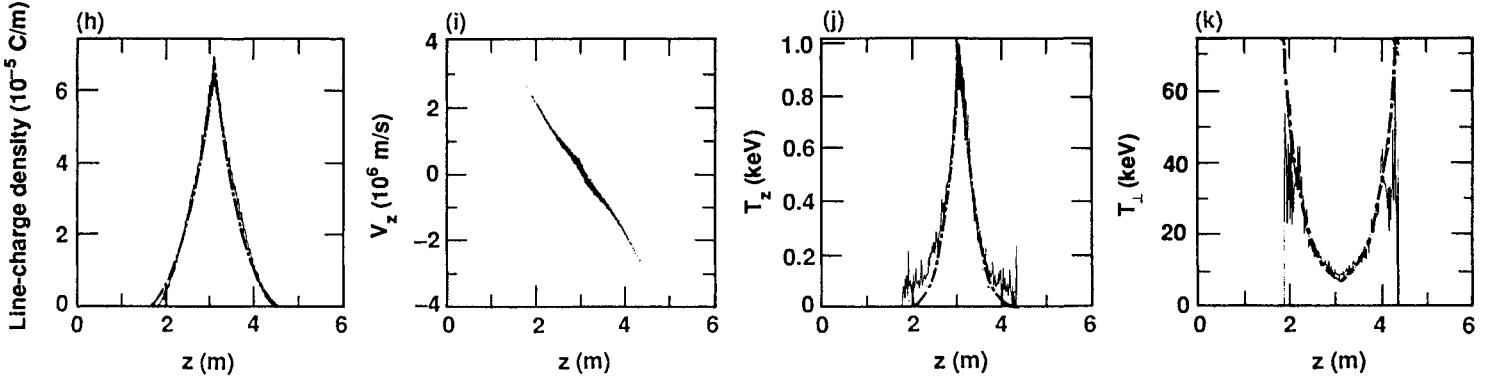

FIGURE 4 (a–g) Beam initial parameters: (a) Line-charge density vs. z. (b) Radial distribution of beam particles vs. z. (c) Particle longitudinal velocities vs. z (in the beam frame). (d) Transverse temperature vs. z. (e) Longitudinal temperature vs. z. (f) Velocity in x-direction vs. x. (g) Normalized rms emittance in x-direction vs. z. (h–k) Beam parameters when the fronts of the rarefaction waves meet at the middle of the beam: (h) Line-charge density vs. z. (i) Particle longitudinal velocities vs. z (in the beam frame). (j) Longitudinal temperature vs. z. (k) Transverse temperature vs. z. (l–r) Beam parameters at the end of compression: (l) Line-charge density vs. z. (m) Radial distribution of beam particles vs. z. (n) Particle longitudinal velocities vs. z (in the beam frame). (o) Transverse temperature vs. z. (p) Longitudinal temperature vs. z. (q) Velocity in x-direction vs. x. (r) Normalized rms emittance in x-direction vs. z.

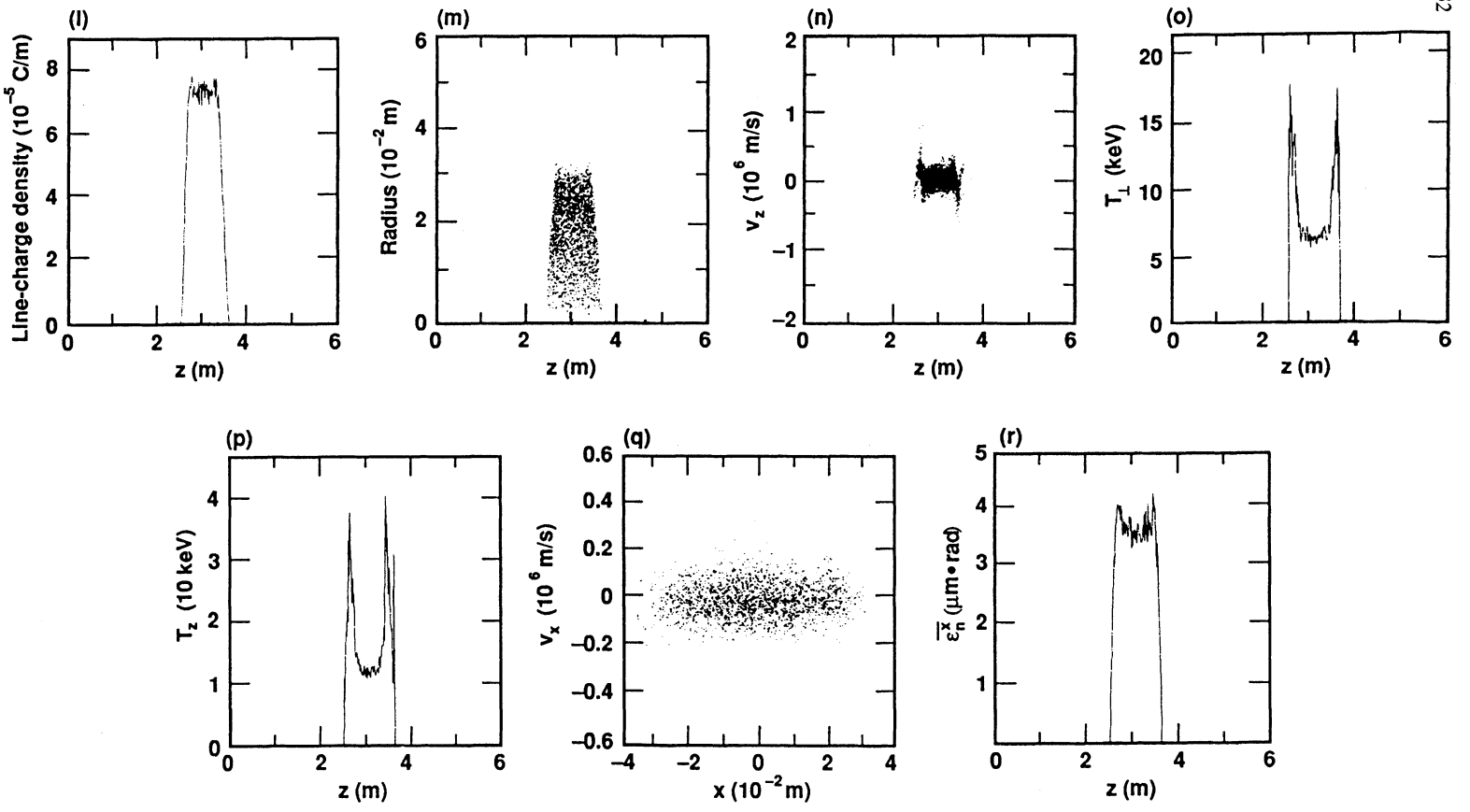

FIGURE 4 (*Concluded*)

normalized rms x emittance $\overline{\varepsilon_n^x}$ is constant along the beam, as shown in Fig. 4g; this plot is also nearly identical to the plot for normalized rms y emittance versus z.

To observe whether there is emittance growth, it is necessary to use normalized emittance ε_n since particles are decelerated along the beam because of the space-charge gradient. The normalized rms emittance in the x direction, measured on the coordinate of any slice along the beam, is given by

$$\overline{\varepsilon_n^x} = \frac{1}{c}[\langle x^2\rangle\langle \dot{x}^2\rangle - \langle x\dot{x}\rangle^2]^{1/2}. \tag{24}$$

Although CONDOR measures emittance on the coordinate moving with the beam center, the normalized emittance obtained from CONDOR for each slice of the beam essentially equals that given by Eq. (24) since the velocity difference between the beam head and beam tail is small compared with the beam-center velocity.

At 0.345 μs after the start, self-compression reduces the beam length to 3 m. At this time, the heads of the rarefaction waves meet at the beam center. The λ profile (Fig. 4h) agrees almost exactly with the result, represented by the dashed line, obtained from Eq. (6) and Fig. 4i shows that the velocity profile has more or less constant slope, as predicted by Eq. (7). The temperatures (Figs. 4j and 4k) vary along the beam essentially according to the adiabatic laws (dashed lines) except near the beam ends.

At 0.735 μs, the beam completes the self-compression and becomes 1 m long. No particles have been lost in the simulation. The line charge density and radial particle distribution become uniform along z except near the ends, as shown in Figs. 4l and 4m. The velocity tilt is essentially removed. However, the line-charge density is about 8% higher than expected from the 1-D theory, i.e., 7.4×10^{-5} C/m instead of 6.88×10^{-5} C/m. The slope of v_z versus z becomes flat (Fig. 4n) and the distribution of v_z is equivalent to having a T_z of 12 keV, except at the ends, as shown in Fig. 4p. The final T_z is 2 keV higher than expected. This temperature is also higher at the two ends because there are a few particles, at the beam ends, that still have high longitudinal velocities relative to the beam center. In other words, the space charge force fails to remove the velocity tilts of the particles near the beam ends. But this effect is not going to have any significant consequences because the total number of particles that still have large velocities is small. The transverse temperature along the beam also decreases, because of radial expansion, and becomes uniform except at the ends as shown in Fig. 4o. Figure 4q shows that there are no longer particles scattered along the v_x axis around $x = 0$ as in Fig. 4f. This is because the particles near the ends of the beam undergo rotation in $v_x - x$ phase space which is caused by radial expansion during the longitudinal compression. The ε_n^x shown in Fig. 4r has approximately the same value, along most of the beam, at the end of the compression as it had at the beginning. However, emittance growth occurs at the ends.

At various stages during the simulation, we plot the radial electric field versus radius at various locations along the beam. On these plots, the electric field lines are coincident straight lines. This indicates that the density is indeed uniform. In all the particle simulations of beam compression, we find that the qualitative behavior of the beam compression does not sensitively depend on small variations, e.g., a few percent, of the initial line-charge density profile and/or velocity profile.

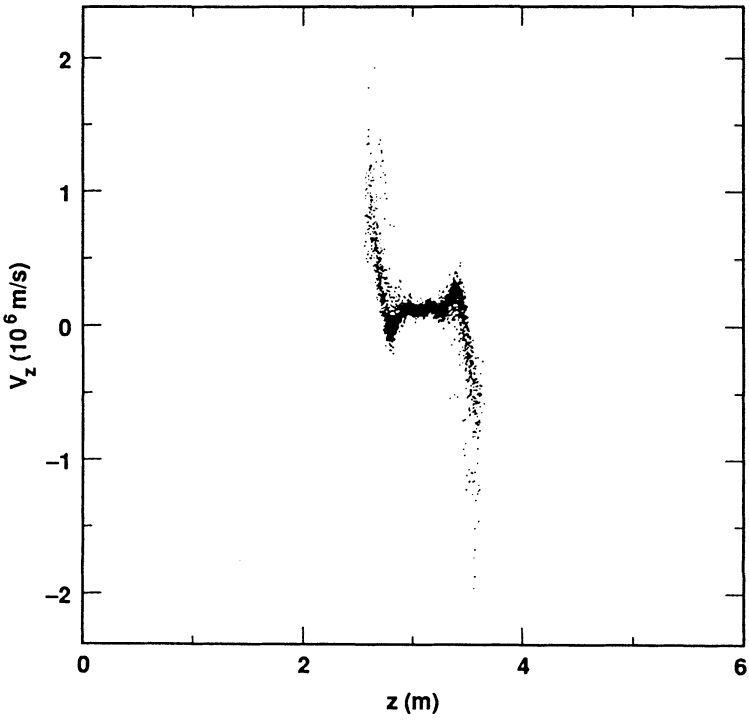

FIGURE 5 Particle longitudinal velocities (in the beam frame) vs. z for zero initial longitudinal temperature.

Finally, we have also carried out a simulation otherwise identical to the one discussed above but with initial $T_z = 0$. Figure 5, taken at 0.735 μs after start, shows that the particle distribution in $v_z - z$ space is along a thin line at the end of the compression. This means that there is no longitudinal emittance growth, except at the ends. However, the time it now taken to compress the beam from 5 m to 1 m is shorter than in the case with nonzero longitudinal temperature since the ends of the beam already start to re-expand, as shown in Fig. 5.

5. CONCLUSION

A scheme has been developed for compressing a heavy-ion beam longitudinally in such a way that the final compressed beam has uniform momentum and line-charge density. Achieving these conditions is important for subsequent focusing of the beam to a small spot radius. The initial line-charge density and velocity-tilt profiles can be approximated by using the self-similar solutions in the simple-wave regions of the beam and using either the approximate solutions described in Section 2 or the method of characteristics in the nonsimple-wave region of the beam. The initial beam manipulation needed to set up the required line-charge density and velocity-tilt profiles can be carried out rapidly enough so that the space-charge effect does not

cause serious degradation of pulse shape. The density profile remains uniform if the initial profile is uniform, even with longitudinal compression.

Particle simulations with the PIC code CONDOR confirm all of the theoretical predictions. Simulations show that the line-charge density and velocity profiles are essentially uniform at the end of compression. Longitudial and transverse temperatures vary along the beam according to the adiabatic laws, and longitudinal and transverse emittance growth is very small and well within the tolerable limits. Scaling laws for beam radius, particle phase advance per period, and FODO system parameters are given for various regions along the drift compression section.

ACKNOWLEDGMENTS

We thank D. L. Judd, R. O. Bangerter, C. M. Celata, K. R. Crandall, A. Faltens, L. J. Laslett, and D. H. Munro for constructive discussions. We are also grateful to P. W. Murphy for editing the manuscript. Work performed under the auspices of the U. S. Department of Energy by the Lawrence Livermore National Laboratory under contract number W-7405-ENG-48.

REFERENCES

1. R. O. Bangerter and D. Keefe, *Nucl. Fusion*, **26**, 1741 (1986).
2. D. J. Dudziak and W. B. Hermannsfeldt, *Heavy Ion Inertial Fusion*, Am. Inst. of Phys. Conf. Proc. 152, M. Reiser, T. Godlove, and R. O. Bangerter, Eds., Washington D.C. (1986).
3. J. Hovingh, V. O. Brady, A. Faltens, D. Keefe, and E. P. Lee, *Fusion Technology* **13**, 255 (1988).
4. L. J. Laslett, Lawrence Berkeley Laboratory Hifar-62, -63, -80.
5. E. P. Lee, *Heavy Ion Inertial Fusion*, Am. Inst. of Phys. Conf. Proc. 152, Washington D.C., 461 (1986).
6. I. Haber, *Proceedings of the Symposium on Accelerator Aspects of Heavy Ion Fusion*, Gesellschaft für Schwerionenforschung, GSI-82-8, Darmstadt, W. Germany, 372 (1982). I. Hofmann and I Bozsik, ibid, 362.
7. J. Bisognano, E. P. Lee, and J. W.-K. Mark, *Laser Program Annual Report 84*, Lawrence Livermore National Laboratory, Livermore, CA, UCRL-50021-84, 3-28 (1985).
8. J. W.-K. Mark, D. D.-M. Ho, S. T. Brandon, C.-L. Cheng, A. T. Drobot, A. Faltens, E. P. Lee, and G. A. Kraft, *Heavy Ion Inertial Fusion*, Am. Inst. of Phys. Conf. Proc. 152, Washington D.C., 227 (1986).
9. D. D.-M. Ho, R. O. Bangerter, J. W.-K. Mark, S. T. Brandon, and E. P. Lee, *Heavy Ion Inertial Fusion*, Am. Inst. of Phys. Conf. Proc. 152, Washington D.C., 243 (1986), and D. D.-M. Ho, R. O. Bangerter, E. P. Lee, S. Brandon, and J. W.-K. Mark, *IEEE Part. Accel. Conf.*, Vol 3 of 3, 1994 (1987).
10. D. D.-M. Ho and S. Brandon, *Nucl. Instrum. Methods*, Vol. A278, No. 1, 182 (1989).
11. L. D. Landau and E. M. Lifshitz, *Fluid Mechanics*, Ch. X (Pergamon Press, Oxford, 1959).
12. A. H. Shapiro, *The Dynamics and Thermodynamics of Compressible Fluid Flow*, Ch. 24 (Ronald, New York, 1953).
13. A. Faltens, E. P. Lee, and S. S. Rosenblum, *Journal of Applied Physics*, **61**, 5219 (1987).
14. D. L. Judd, Lawrence Berkeley Laboratory, Berkeley, CA, private communication (1989).
15. A. Faltens, Lawrence Berkeley Laboratory, Berkeley, CA, private communication (1987).
16. E. P. Lee, T. J. Fessenden, and L. J. Laslett, *IEEE Trans. Nucl. Sci.*, **32**, 2489 (1985).
17. M. Reiser, *Part. Accelerators*, **8**, 167 (1978).
18. I. Hofmann and J. Struckmeier, *Part. Accelerators*, **21**, 69 (1987).
19. M. Reiser, C. R. Chang, D. Kehne, K. Low, and T. Shea, *Phys. Rev. Lett.*, **61**, 2933 (1988); T. P. Wangler, Los Alamos National Laboratory memorandum AT-1: 84–323 (1984).
20. O. A. Anderson, *Part. Accelerators*, **21**, 197 (1987).
21. K. D. Hahn, Lawrence Berkeley Laboratory, LBL-26167, 1989.
22. P. R. Garabedian, *Partial Differential Equations* (Wiley, 1964).
23. I. Hofmann, L. J. Laslett, L. Smith, and I. Haber, *Part. Accelerators*, **13**, 145 (1983).
24. M. G. Tiefenback, *Space-Charge Limits on the Transport of Ion Beams in a Long Alternating Gradient System*, Ph.D. Thesis, Univ. of Calif., Berkeley and LBL-22465 (1986).

APPENDIX A Obtaining Fluid Properties of the Beam Using the Method of Characteristics

The characteristics meshes shown in Figs. 6a and 6b provide a convenient way to obtain the λ and v_z profiles of the beam. By using this method, one can obtain the beam properties without running a complicated computer code every time. This method also provides a check to the approximate solution in the nonsimple-wave region given in Section 2. This Appendix first gives a brief discussion of the theory underlying the method of characteristics, then outlines the procedure for constructing the characteristics meshes, and finally compares the result obtained from the characteristics meshes to that obtained from particle simulation. (For a detailed physical treatment of the method of characteristics, see Refs. 11 and 12. For a detailed mathematical treatment, see Ref. 22).

To construct the characteristic meshes, we need to obtain the Riemann invariants. Define function σ so that $d\sigma/d\lambda = c/\lambda$. Substituting this relation into Eqs. (1) and (2) we obtain

$$\frac{\partial \sigma}{\partial t} + v_z \frac{\partial \sigma}{\partial z} + c \frac{\partial v_z}{\partial z} = 0, \tag{A-1}$$

$$\frac{\partial v_z}{\partial t} + v_z \frac{\partial v_z}{\partial z} + c \frac{\partial \sigma}{\partial z} = 0. \tag{A-2}$$

Adding and subtracting these two equations give

$$\left[\frac{\partial v_z}{\partial t} + (v_z + c)\frac{\partial v_z}{\partial z}\right] \pm \left[\frac{\partial \sigma}{\partial t} + (v_z + c)\frac{\partial \sigma}{\partial z}\right] = 0. \tag{A-3}$$

Thus the functions

$$J_\pm = v_z \pm \int \frac{c\, d\lambda}{\lambda},$$

$$= v_z \pm 2c, \tag{A-4}$$

are invariants along the trajectories

$$\left(\frac{dz}{dt}\right)_\pm = v_z \pm c. \tag{A-5}$$

Here, $J_\pm$ are called the Riemann invariants and $v_z + c$ and $v_z - c$ are called C_+ and C_- characteristics, respectively. These characteristics on the (z, t) plane (the "physical plane") are called the "physical characteristics" in the literature of compressible fluid dynamics.[12]

Differentiating Eq. (A-4) gives

$$\left(\frac{dc}{dv_z}\right)_\pm = \mp\tfrac{1}{2}. \tag{A-6}$$

Thus, the "state characteristics," i.e., the characteristics on the (v_z, c) plane (the "state plane"), are straight lines.

We now illustrate the procedure of obtaining the characteristics meshes by numerically integrating Eqs. (A-5) and (A-6). (This procedure is identical to that of obtaining the characteristics meshes for an ideal gas with $\gamma = 2$.) The problem under consideration is a uniform beam of length $2L$. Because of the symmetry of the problem, the right half of the beam can be replaced by a solid wall at $z = 1$. It is useful first to normalize the variables; let

$$Z = \frac{z}{L}, \qquad t = \frac{c_0 t}{L},$$
$$V_z = \frac{v_z}{c_0}, \qquad C = \frac{c}{c_0}. \tag{A-7}$$

Equations (A-4) allow us to rewrite Eqs. (A-5) as

$$\left(\frac{dz}{dt}\right)_+ = \tfrac{3}{4}J_+ + \tfrac{1}{4}J_-,$$
$$\left(\frac{dz}{dt}\right)_- = \tfrac{1}{4}J_+ + \tfrac{3}{4}J_-. \tag{A-8}$$

In the simple-wave region, dz/dt for a given characteristics remains constant since one of the Riemann invariants is a constant throughout the simple-wave region.

For the present problem, the characteristics radiate away from the point $z = 0$ and $t = 0$ in the form of an expansion fan. The leading-edge of the fan expands into the undisturbed region ($V_z = 0$, $C = 1$) on the right at speed c_0, and the trailing-edge of the fan expands into the vacuum region ($C = 0$) on the left at the escape speed $-2c_0$. To construct the characteristics mesh, we choose the C_+ characteristics inside the expansion fan in such a way that the absolute difference in V_z between any of the neighboring characteristics is 0.05, as shown in Fig. 6a. In the figure, each characteristic is specified by a number. The way that these numbers are chosen is described in Ref. 12. The plus or minus sign after each number refers to the families of C_+ and C_- characteristics, respectively. The slope of a C_+ characteristic starts to change when it encounters a C_- characteristic with different values of J_-.

To construct the characteristics in the nonsimple-wave region on the physical plane, note that at point b we have $V_z = 0$ and we know J_+, so that J_- and the slope of C_- can be determined. Similarly, all the values of J_- along different C_- characteristics can be determined; thus, the slopes of C_+ and C_- at each intersection point of these families of characteristics can be found. To improve the accuracy of construction, the slope of the characteristics between two connecting points is taken to be the average of the slopes at the two connecting points. Thus, using a hand calculator and starting from point b, we construct the characteristics mesh by locating every intersecting point of the C_+ and C_- characteristics in a stepwise fashion, migrating toward the directions of increasing t and decreasing z. Note that the C_- characteristic that separates the simple wave and the wave interacting regions can be expressed as[11]

$$Z = -2t + 3t^{1/3}, \quad t \geq t_0, \tag{A-9}$$

which is line ab on Fig. 6a.

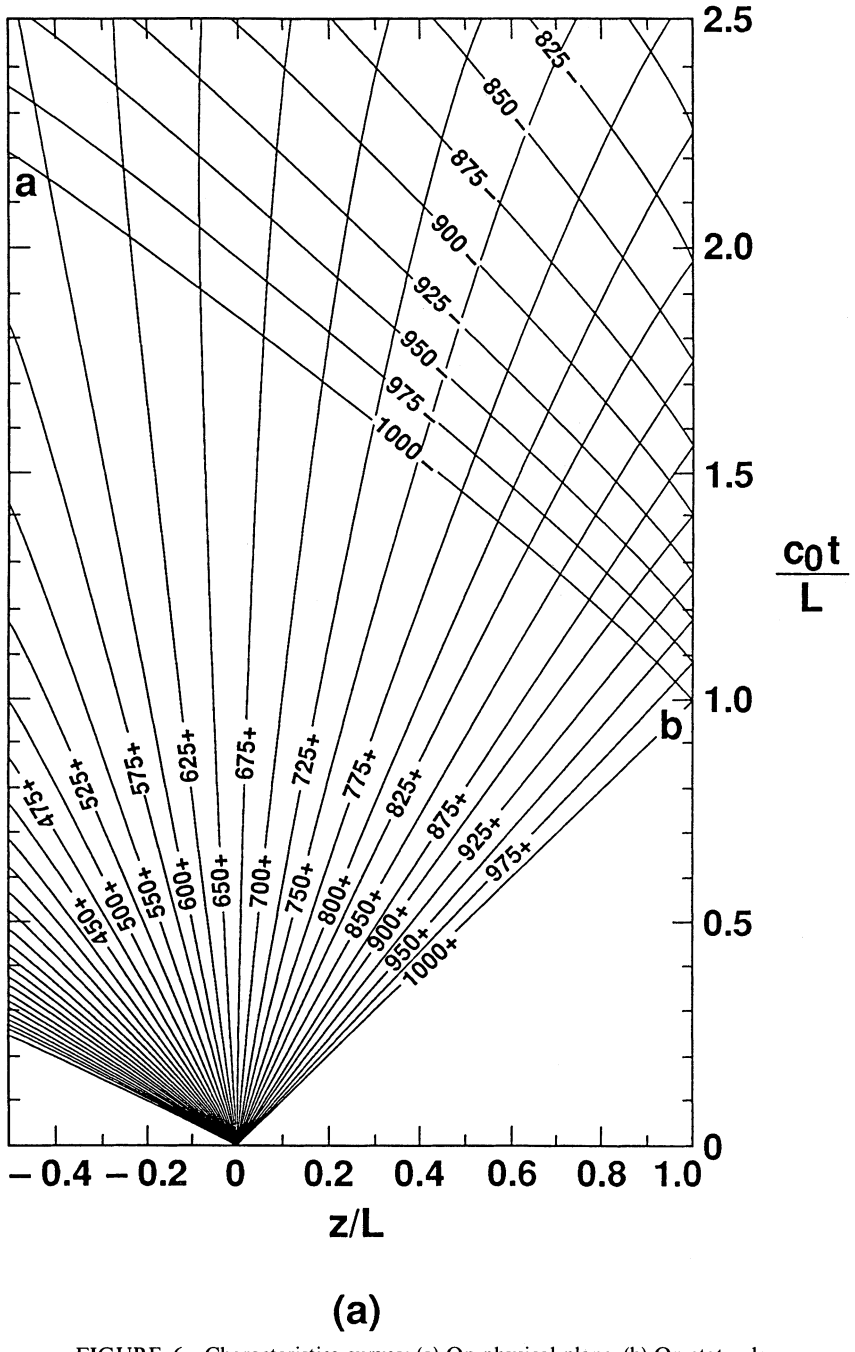

(a)

FIGURE 6 Characteristics curves: (a) On physical plane. (b) On state plane.

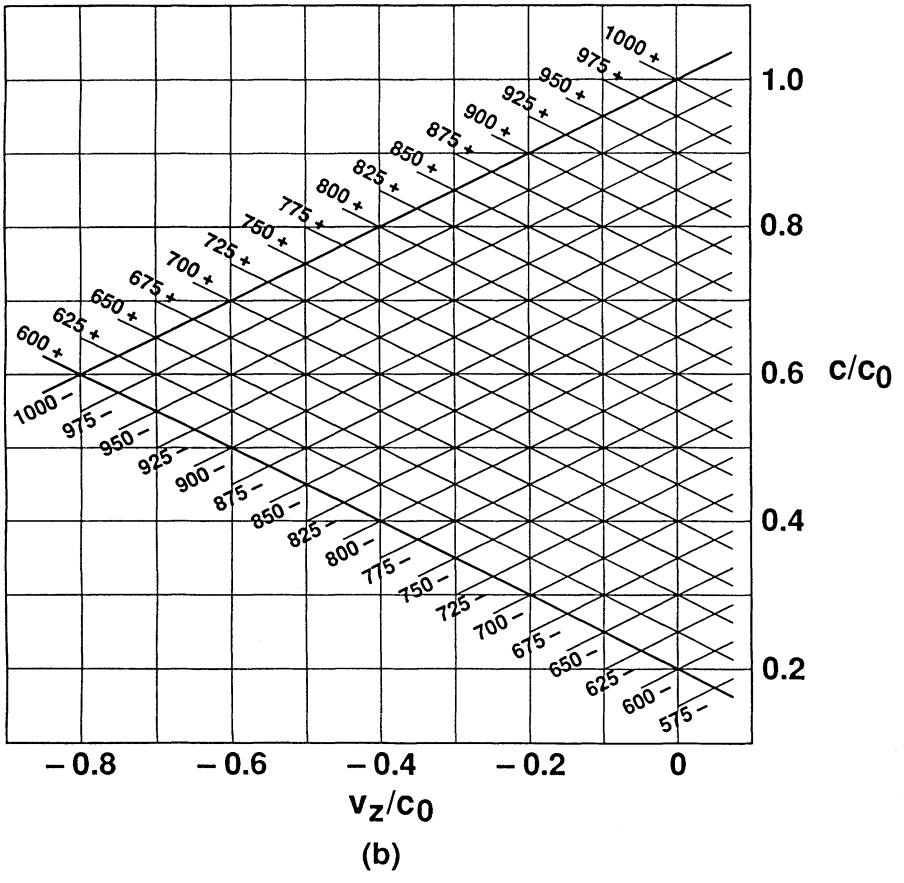

FIGURE 6 (*Concluded*)

The characteristics on the state plane (Fig. 6b) are simply two families of straight lines with opposite slopes given by Eq. (A-6). Each characteristics is assigned a number that corresponds to the C_+ and C_- characteristics in Fig. 6(a) with the same number.

From Figs. 6a and 6b, the entire flow pattern, in terms of velocity distribution, may be determined. Using the Riemann invariants and the adiabatic relations, the rest of the fluid properties of the beam can be obtained for all times. Note that all the simulations show that velocity profile in the nonsimple-wave region has a slope that is essentially constant (in space; it varies in time). The reason is explained later in this appendix. This fact simplifies the task of locating the values of V_z and C on the state plane.

Using this method, the initial flow pattern of the 5-m-long beam used for particle simulation, as shown in Figs. 2, 4a, and 4c, is determined. The accuracy of this method of determining the evolution of the flow pattern is manifested by the close agreement between the line-charge density profile obtained from this method to that obtained by particle simulation described in Section 4. This agreement is further supported by the close agreement between theory and experiment.[13]

Two reasons can be advanced for the close agreement between the results from the characteristics meshes and the particle simulation discussed in Section 4, despite the fact that the g factor is treated as a constant independent of z in the construction of the characteristics meshes and in obtaining the simple wave solution [Eqs. (6) and (7)]. First, the beam radius does not change significantly in the nonsimple-wave region. Therefore the g factor in the nonsimple-wave region does not vary significantly. Second, the dominant contribution of the action on particles due to the $\partial\lambda/\partial z$ force occurs near the boundaries that separate the nonsimple- and simple-wave regions. Hence, although the beam radius and consequently the g factor both vary considerably in the simple-wave regions, the influence of the g factor on beam dynamics is less significant in these regions.

Finally, as mentioned in Section 2.1, the C_+ and C_- characteristics in the nonsimple-wave region are very close to straight lines and therefore the velocity is expected to be nearly linear in z in this region as long as t is not very much larger than t_0. This is so because if the characteristics in this region were indeed straight lines, this means that the characteristics would not interact with each other. Therefore, the velocity in this region is linear from superposition.

APPENDIX B Beam Transport Scaling Laws in the FODO System During Longitudinal Compressions

The beam length is reduced by an order of magnitude during compression and some of the beam parameters therefore also change substantially. To compensate for these changes, the FODO parameters must also vary along the drift compression section.

The transport scaling laws are presented in the first part of this appendix. An estimate of the total length of a typical beam compression section is given in the second part.

When the beam enters the drift-compression section, there may be considerable clearance between the beam edge and the aperture radius of the magnetic quadrupoles. Thus, during the first part of the drift compression, we can let the FODO parameters be fixed, while the beam radius increases until the clearance reaches some tolerance-related limit (determined, e.g., by image force, misalignment, or aberration).

To investigate the change in the beam intensity during this stage of drift compression, we study the evolution of σ/σ_0. Note that the unnormalized emittance[17]

$$\varepsilon \simeq \frac{\sigma}{\sigma_0} a^2 k_0^{1/2}, \tag{B-1}$$

is constant at the beam center (because of vanishing velocity tilt). We therefore have

$$\left.\frac{\sigma}{\sigma_0}\right|_{z=0} \propto \frac{1}{Q(z=0,t)}. \tag{B-2}$$

When the limit for the clearance between the beam edge and the aperture radius is reached, one can either increase $\overline{k_0}$, to prevent further expansion of the beam radius, or increase the aperture radius. We choose the first option.

First let $\overline{k_0}$ be fixed, but allow η and l to vary. At the point at which the beam enters the drift compression section, η is normally small (e.g., $\eta \leq 1/5$). Since η may have an upper limit of about 1/3 as a result of beam bending considerations, i.e., the value of η is limited in order to provide enough space for bending magnets, we can increase $\overline{k_0}$ by increasing η to keep the beam radius fixed. Changes in η and l must always satisfy the constraint[16,17]

$$\sigma_0 = \sqrt{\frac{3-2\eta}{3}}\,\eta k_0 l^2 \leq 90^\circ, \tag{B-3}$$

to avoid envelope instabilities.[23] Initially, we fix σ_0 at 90°. This allows us to write

$$\begin{aligned} \sqrt{\eta(z)}[3-2\eta(z)]^{1/4} &\propto \sqrt{Q(z=0,t)}, \\ l &= \frac{\text{const.}}{\sqrt{\eta(z)}[3-2\eta(z)]^{1/4}}, \\ \left.\frac{\sigma}{\sigma_0}\right|_{z=0} &\propto \frac{1}{\sqrt{Q(z=0,t)}}. \end{aligned} \tag{B-4}$$

When η reaches the upper limit, it may still be possible to keep the beam radius fixed by increasing the pole-tip magnetic field B_0 (if the engineering limit on B_0 has not been reached). Again, to keep σ_0 at 90°, one can show that

$$\begin{aligned} \sqrt{B_0(z)} &\propto \sqrt{Q(z=0,t)}, \\ l &= \frac{\text{const.}}{\sqrt{B_0(z)}}, \\ \left.\frac{\sigma}{\sigma_0}\right|_{z=0} &\propto \frac{1}{\sqrt{Q(z=0,t)}}. \end{aligned} \tag{B-5}$$

Of course, these two procedures for keeping the beam radius constant by increasing η or B_0 while decreasing l can be carried out in reverse order, or as a single step.

Once the limits on η and B_0 are reached, it is necessary to increase the aperture radius while the beam is still undergoing drift compression. If we assume that the ratio of aperture radius to beam radius is fixed in this region, and that $\sigma_0 = 90^\circ$, we can show that

$$\begin{aligned} a &\propto Q(z=0,t), \\ \frac{l}{\sqrt{a}} &= \text{const.}, \\ \left.\frac{\sigma}{\sigma_0}\right|_{z=0} &\propto \frac{1}{[Q(z=0,t)]^{3/2}}. \end{aligned} \tag{B-6}$$

After the line charge density profile reaches the shape shown in Fig. 1g, the line charge density at $z = 0$ will remain fixed, so that there is no further need to

change any of the FODO structure until the end of the drift compression section. Note that Eqs. (B-2), (B-4), and (B-5) show that σ/σ_0 always decreases during compression. Thus, it is important to carry out beam transport experiments with tune depression less than that already achieved in the single-beam-transport experiment (SBTE) which has the lowest value of σ/σ_0 between 0.1 and 0.2.[24]

Finally, we estimate the length of the compression for the beam with parameters given in Table I. From the simulation presented in Section 4, it takes 0.75 μs to compress the beam from 5 m to 1 m. Thus, it takes about 2.6 μs to compress the beam from 15 m to 1 m. If the beam travels at 1/3 the speed of light, then the distance travelled by the beam during longitudinal drift compression from 15 m to 1 m is about 260 m.